Optimization of a Liquid-Cooled Lithium-Ion Battery Pack for Electric Aircraft Based on an Integrated Electro-Thermal-Aging Pack Model

Liang, Yawen; Luo, Weiming; Mouli, Gautham Ram Chandra; Bauer, Pavol

DOI
10.1109/TTE.2025.3586087

Publication date
2025

Document Version
Final published version

Published in
IEEE Transactions on Transportation Electrification

Optimization of a Liquid-Cooled Lithium-Ion Battery Pack for Electric Aircraft Based on an Integrated Electro-Thermal-Aging Pack Model

Yawen Liang, *Graduate Student Member, IEEE*, Weiming Luo, Gautham Ram Chandra Mouli, *Member, IEEE*, and Pavol Bauer, *Senior Member, IEEE*

***Abstract*— Electric aircraft represent a promising low-emission alternative to fuel-powered aviation. As the energy source, the battery pack must guarantee key performance metrics such as energy density, power density, lifetime, and safety. Among these, energy density is particularly critical as it directly impacts the range and payload capacity. Additionally, the battery thermal management system (BTMS) of the battery pack is essential to maintain safety, efficiency, and lifetime. Hence, to design a battery pack with improved energy density and optimized thermal and aging performance, a complete electro-thermal-aging (ETA) model at both cell and pack levels is developed to predict pack behavior under operational conditions. Simulations demonstrate that the proposed model achieves an accurate thermal prediction accuracy within 0.87°C during an example all-electric aircraft (AEA) mission profile. Optimization based on the proposed model is conducted, focusing on geometric configurations of the battery pack and coolant flow parameters, including channel wall thickness (L_{Al}), inlet width (W_{cl}), cell spacing (D_{cell}), package wall thickness (L_{enc}), inlet flow temperature ($T_{\mathrm{cl,in}}$), and flow velocity ($U_{\mathrm{cl,in}}$). An optimized liquid-cooled battery module using Samsung 18650-35E cells is designed with $[L_{\mathrm{Al}}, W_{\mathrm{cl}}, D_{\mathrm{cell}}, L_{\mathrm{enc}}] = [0.4, 1.6, 20, 0.5]$ mm, $T_{\mathrm{cl,in}} = 35$°C, and $U_{\mathrm{cl,in}} = 0.05\,\mathrm{m\,s^{-1}}$ during cruise and $0.02\,\mathrm{m\,s^{-1}}$ during takeoff, climb, and descent. This configuration achieves a maximum temperature of 41.76°C and a maximum cell-to-cell temperature difference of 3.11°C, improving thermal uniformity. The lifetime performance also demonstrates a 5.51% improvement in state of health (SOH) after 180 cycles. Based on the module-to-pack structure analysis, the battery pack exhibits energy densities of 227.01 $\mathrm{W\,h\,kg^{-1}}$ gravimetrically and 353.67 $\mathrm{W\,h\,L^{-1}}$ volumetrically. This study facilitates the guideline for compact and lightweight liquid-cooled battery pack design with improved thermal and aging performance for AEA applications.**

***Index Terms*— Battery thermal management system (BTMS), electric aircraft, electro-thermal-aging (ETA) model, liquid-cooled lithium-ion battery (LIB) pack.**

Received 7 March 2025; revised 3 June 2025; accepted 27 June 2025. Date of publication 4 July 2025; date of current version 25 September 2025. This work was supported in part by European Union's Horizon 2020 Research and Innovation Program under Grant 101036996. *(Corresponding author: Yawen Liang.)*

Yawen Liang, Gautham Ram Chandra Mouli, and Pavol Bauer are with the Electrical Sustainable Energy Department, Delft University of Technology, 2600 AA Delft, The Netherlands (e-mail: y.liang-3@tudelft.nl; g.r.chandramouli@tudelft.nl; p.bauer@tudelft.nl).

Weiming Luo was with the Electrical Sustainable Energy Department, Delft University of Technology, 2600 AA Delft, The Netherlands. He is now with the Department of Battery System Development (BSD)-Thermal Management System (TMS), Contemporary Amperex Technology Company Ltd. (CATL), Ningde 352107, China (e-mail: weimingluostu@163.com).

This article has supplementary downloadable material available at https://doi.org/10.1109/TTE.2025.3586087, provided by the authors.

Digital Object Identifier 10.1109/TTE.2025.3586087

NOMENCLATURE

AC	Aging submodel at the cell level.
AEA	All-electric aircraft.
BMS	Battery management system.
BTMS	Battery thermal management system.
CFD	Computational fluid dynamics.
CCCV	Constant current constant voltage.
ECM	Electrical circuit model.
EC	Electrical submodel at the cell level.
EP	Electrical submodel at the pack level.
ETA	Electro-thermal aging.
HCE	Heat conducting element.
LIB	Lithium-ion battery.
MAE	Mean absolute error.
OCV	Open-circuit voltage.
PCM	Parallel cell module.
RMSE	Root-mean-square error.
SCM	Series cell module.
SOC	State of charge.
SOH	State of health.
TC	Thermal submodel at the cell level.
TP	Thermal submodel at the pack level.

I. INTRODUCTION

THE growing demand for emission reductions has significantly accelerated the development and adoption of electric aircraft. As a promising alternative to conventional fuel-powered aviation, electric aircraft offer substantial benefits, including lower greenhouse gas emissions and improved operational efficiency. For battery-powered electric aircraft, LIBs stand out among various battery chemistries due to their high energy density, well-established technology, and strong battery supply chain, making them a viable choice for immediate implementation. These attributes position LIBs as the optimal choice for short-range AEA, which are expected to dominate the electric aviation landscape in the near future [1].

However, the substantially lower energy density of batteries compared to aviation and jet fuels remains a significant challenge. Furthermore, the performance of LIBs, including lifetime, internal resistance, and safety, is highly dependent on operating temperature. In AEA applications, battery lifetime is especially critical, as cell aging directly reduces the range, payload capacity, and power output [2]. Additionally, the increased internal resistance reduces efficiency and increases

TABLE I
SUMMARY OF RELATED STUDIES

Ref.	EC	TC	AC	EP	TP	Electrical effect on TC	Electrical effect on AC	Thermal effect on EC	Thermal effect on AC	Aging effect on EC	BTMS
[6]	✓	✓	✓	✓	✓	✓	✓	✓	✓		Air-cooled
[8]	✓		✓	✓			✓	✓		✓	
[9]	✓	✓	✓		✓	✓		✓	✓	✓	Free convection
[10]	✓	✓		✓	✓	✓		✓			Liquid-cooled
[11]	✓	✓	✓	✓	✓	✓	✓		✓		Air-cooled
[12]	✓	✓			✓	✓		✓			Hybrid BTMS liquid-phase change material
[13]		✓			✓	✓		✓			Hybrid BTMS liquid-phase change material
Our model	✓	✓	✓	✓	✓	✓	✓	✓	✓	✓	Liquid-cooled

the battery's heat generation rate. A compact and lightweight BTMS can improve the specific energy of the battery pack and reduce the overall weight of the aircraft, thus improving its payload and range capability. Moreover, an effective BTMS is essential for maintaining the optimal operating temperature of LIB packs [3]. Due to the high computational cost of CFD simulations, an ETA pack model is needed, which can provide an effective and computationally efficient solution for performing dynamic thermal and lifetime performance analysis while requiring minimal computational resources. Based on this pack model, an optimal BTMS can be designed, focusing on enhanced control of maximum temperature, improved temperature uniformity, and increased gravimetric and volumetric energy density.

A. Related Work

1) Battery Pack Model: The battery pack model is not simply aggregating individual cell models to create the battery pack model because cell parameters, including battery capacity and internal resistance, exhibit variations from cell to cell due to manufacturing variances. In addition, thermal and electrical interactions between individual battery cells cannot be eliminated, which can lead to distinct operational conditions and nonuniform degradation among cells [4], [5], [6], [7].

Several research papers have specifically focused on modeling the battery pack. In [6], an ETA coupling model for the single battery cell is proposed first. This is followed by integrating an air-cooling pack model and a battery pack equilibrium management model for the comprehensive battery pack model. Dubarry et al. [8] presented a pack model by integrating various submodels from previous publications, which includes a submodel of the ECM for a single battery cell, a submodel to predict the cell voltage response under different degradation paths, a submodel for cell-to-cell variations, and submodels for cell imbalances and BMS. Lucero et al. [9] proposed an electrothermal battery pack model that accounts for heat exchange between the battery cell, module, pack, and ambient air. This study integrated a semi-empirical aging model and investigated the impact of cell-to-cell capacity variations. In [10], electrochemical-thermal interactions within battery packs were modeled, enabling fast and detailed simulations across various BTMS designs and pack configurations. In [11], the control-oriented multitimescale battery pack model is based on the interaction between system models of the electrical and thermal dynamics, along with models of cell aging dynamics, while considering the electrical topology, thermal management, and cell-to-cell manufacturing variability. He et al. [12] present a lumped electrothermal model for a hybrid cooling battery pack. This model enables the prediction of temperature variations between individual cells using a hybrid cooling BTMS. Similarly, Lebrouhi et al. [13] developed a cost-effective lumped model to simulate a battery pack with liquid-phase change material BTMS undergoing continuous charging and discharging cycles.

The summary of the related studies is shown in Table I, where EC, TC, and AC represent the electrical, thermal, and aging submodels at the battery cell level, respectively. EP and TP models denote the electrical and thermal submodels at the pack level, respectively. As shown in Table I, only part of the interactions are covered in existing models.

2) BTMS Design: In [14], an optimization design framework was proposed to minimize the maximum temperature difference in an LIB pack with a serpentine cooling channel. This was achieved by optimizing parameters that include the channel inlet width, channel wall thickness, coolant velocity, and coolant temperature. In [15], a meandering-type wavy cooling tube was designed for an 18650 battery pack to evaluate the thermal performance of ternary hybrid nanofluid as the coolant. The effects of different nanofluid compositions, dispersant dosages, mass fractions, and flow rates were investigated. Al-Haddad et al. [16] designed an air-cooled battery pack to maintain uniform temperature distribution, employing a neural network model to predict the heat flux within individual battery cells. Sadeh et al. [17] designed a hybrid BTMS that combines both direct and indirect liquid cooling for a 21700 battery pack. The study examined the effects of immersion and flow-based cooling methods, inlet flow velocities in cooling channels and tubes, parallel and counter flow, and cell spacing on the battery thermal performance.

The compactness and weight of the BTMS are crucial for battery packs in AEAs. Lai et al. [18] focused on a compact and lightweight BTMS design to effectively control the maximum temperature and temperature difference of a lithium-ion power battery pack. An et al. [19] proposed a lightweight honeycomb hybrid BTMS that integrates multilayered liquid-cooling channels into a 3-D-printed metal scaffold to enhance the thermal exchange performance. The study analyzed the effects of coolant inlet and outlet configuration, the number of channel layers, porosity, coolant flow rate, and continuous charge-discharge cycling on overall heat dissipation. In [20], a compact and lightweight hybrid BTMS for prismatic LIBs was designed, combining phase change

materials with liquid cooling in a honeycomb-like configuration. Thakur et al. [21] proposed a liquid-cooled BTMS incorporating HCEs with three curved surfaces and a central liquid flow channel. These HCEs are strategically arranged to form a compact structure within the battery pack for weight reduction. The study further investigated the influence of key design parameters, specifically the surface contact angle and height of the HCEs along the coolant flow direction. The performance of the BTMS designs in all the aforementioned studies was evaluated through numerical simulations using commercial CFD software.

Hence, research on BTMS design often overlooks the tradeoff between thermal performance and energy density, particularly both gravimetric and volumetric energy density. Moreover, while BTMS optimization has made progress in recent years, optimization using analytical models without relying on time-consuming numerical CFD simulations remains an open problem. Specifically, the optimization of liquid-cooled battery packs for AEA, based on predictions of ETA performance, while paying attention to the weight of the BTMS and hence the energy density at pack level, has yet to be investigated in the available literature.

B. Contribution

Compared with existing studies, this article has five main contributions.

1) An empirical aging model for cycling degradation, tailored explicitly for high-energy-density INR1860-35E LIBs, is proposed using a publicly available battery cycling dataset. The model accounts for dependencies on temperature, C-rate, and throughput.
2) An electrical pack model based on Kirchhoff's law is proposed, which considers both SCM and PCM topologies and accommodates input sources as either voltage or current.
3) A thermal pack model that includes the cell SOC, cell temperature, cell aging status, and current-dependent heat generation model, along with the heat transfer model for the liquid-cooling system, is developed.
4) An integrated ETA model is developed, combining all the submodels and capturing interactions between cell temperature, current, SOC, SOH, pack geometric parameters, coolant velocity, and coolant temperature.
5) An optimization framework for the BTMS design is proposed, considering the unique power profile of AEA, including takeoff, climb, cruise, and descent phases, as well as ambient temperature variations with altitude, to optimize both thermal performance and energy density of the battery pack.

C. Article's Structure

This article is structured as follows. Section II presents the ETA battery model at the cell level. Section III explores the battery pack design. Besides, electrical and thermal interactions at the pack level are investigated. In Section IV, the BTMS optimization is discussed, focusing on thermal performance and energy density. Finally, Section V concludes this study.

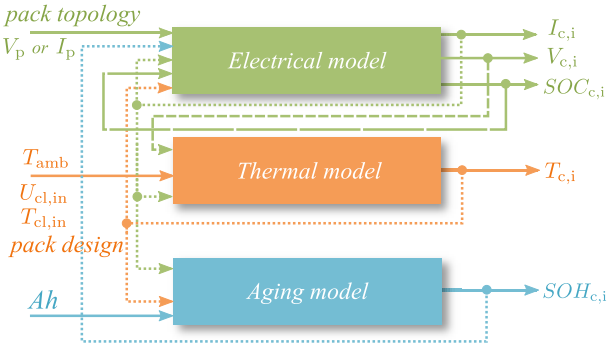

Fig. 1. Integrated ETA pack model.

II. Battery Cell Model

The integrated ETA pack model developed for AEA BTMS optimization is shown in Fig. 1. The model consists of three interconnected submodels. The electrical submodel predicts the battery cell voltage, current, and SOC in response to the pack current or voltage, pack topology, and cell temperature and degradation status. The thermal submodel calculates the cell temperature as a function of cell current, voltage, ambient temperature, and BTMS parameters. Finally, the aging submodel estimates capacity fade based on cell operating conditions, including charge throughput (Ah), cell temperature, and cell current. To achieve this, a cell-level model is required first. This section elaborates on the battery cell model, covering its electrical, thermal, and aging aspects.

A. Electrical Submodel

1) Electrical Circuit Model: In this study, the electrical submodel adopts the second-order RC Thévenin-based model, as illustrated in Fig. 2. This ECM incorporates multiple components, including the OCV $V_{\mathrm{OCV,c}}$, the ohmic resistance R_o, the short-time transient parallel RC pair R_s and C_s, and the long-time transient parallel RC pair R_l and C_l. The OCV represents the voltage of a fully relaxed battery cell. The ohmic resistance R_o accounts for the internal resistance of the battery cell, encompassing surface layer resistance and bulk resistance, which contributes to instantaneous voltage fluctuations. The short-time transient components R_s and C_s capture the fast dynamics within the battery, such as activation polarization. Conversely, the long-time transient components R_l and C_l represent concentration polarization. If the input is a current source, the equations for the ECM can be expressed as follows:

$$\begin{aligned} V_l(t) &= I_{l1}(t)R_l = I_{\mathrm{c}}(t)R_l\left(1-e^{-\frac{t}{R_lC_l}}\right) \\ V_s(t) &= I_{s1}(t)R_s = I_{\mathrm{c}}(t)R_s\left(1-e^{-\frac{t}{R_sC_s}}\right) \end{aligned} \tag{1}$$

where $I_{\mathrm{c}}(t)$ is the battery cell current, which is split between the resistor current I_{s1} and I_{l1} and the capacitor current I_{s2} and I_{l2}.

Alternatively, if the input is a voltage source, the equations for the continuous form of the ECM are presented as follows:

$$\begin{aligned} V_l(t) &= I_{l1}(t)R_l = \frac{1}{C_l}\int (I_{\mathrm{c}}(t) - I_{l1}(t))dt + V_{l2,0} \\ V_s(t) &= I_{s1}(t)R_s = \frac{1}{C_s}\int (I_{\mathrm{c}}(t) - I_{s1}(t))dt + V_{s2,0} \end{aligned} \tag{2}$$

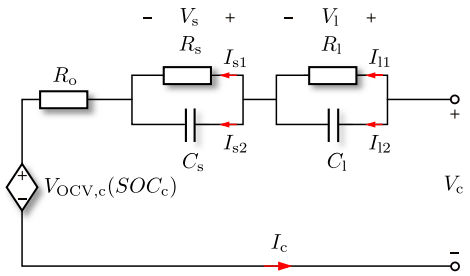

Fig. 2. Second-order *RC* Thévenin-based model.

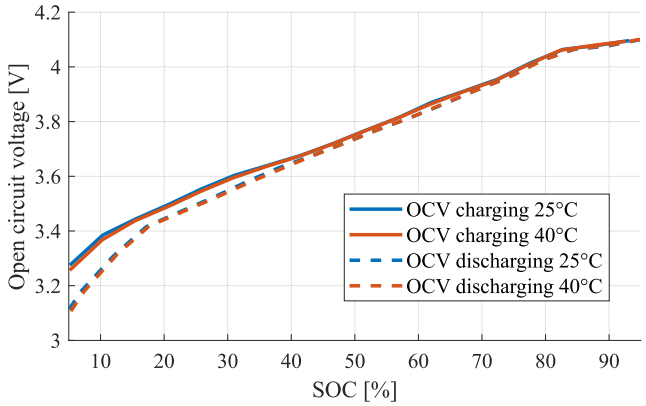

Fig. 3. OCV under different SOC and temperature conditions.

where $V_{l2,0}$ and $V_{s2,0}$ are the initial voltage value of the short-time transient parallel *RC* pair and the long-time transient parallel *RC* pair, respectively.

Whether the input source is a voltage or a current source, the battery cell voltage and SOC are expressed as shown in the following equation:

$$\begin{aligned} V_c(t) &= V_{OCV,c}(t) + I_c(t)R_o + V_s(t) + V_l(t) \\ \mathrm{SOC}_c(t) &= \frac{\int I_c(t)dt}{S_f} + \mathrm{SOC}_{c,0} \end{aligned} \tag{3}$$

where $V_c(t)$ is the terminal voltage of the battery cell, S_f is the full battery capacity, $\mathrm{SOC}_c(t)$ is the real-time battery cell SOC, and $\mathrm{SOC}_{c,0}$ is the initial SOC.

2) Varying Parameter of the Second-Order RC Thévenin-Based Model: The parameters of the second-order *RC* Thévenin-based model are complex functions influenced by multiple variables, such as SOC, temperature (T), current direction, C-rate (defined as the battery charge or discharge current normalized by its rated capacity), battery aging status (SOH), self-discharge rate, and hysteresis effects [22]. In this study, the ECM parameters are modeled as a function of SOC, T, C-rate, and SOH, which is essential for accurately predicting battery behavior [23]. These parameters are experimentally determined using a current pulse test. The current pulse test under different C-rates (from 0.2 C to 1.0 C) and ambient temperatures (0 °C, 10 °C, 20 °C, 25 °C, 30 °C, and 40 °C) was conducted in previous work [24]. Details of the current pulse test profile are provided in supplementary material Section 2.1. In the experiment, the Samsung INR18650-35E cylindrical cell is chosen as a representative of the NMC technology of LIBs. The key parameters of the tested battery cell are outlined in supplementary material Table I [25]. The same current pulse test profile was repeated at different SOH levels from 1 to 0.9, for three INR18650-35E cells. The measurement results were curve-fit to derive the ECM components as functions of SOC, T, C-rate, and SOH, as detailed in supplementary material Section 2.2.

B. Thermal Submodel

1) Heat Generation Model: The thermal model of the battery cell comprises the heat generation and transfer models. For battery cells inside the liquid-cooled battery pack, heat dissipation is influenced by the coolant and ambient air, cell position, and neighboring cells, as discussed in Section III-C. Therefore, this section focuses only on heat generation.

In this thermal model, the heat generation and temperature within the battery cell are assumed to be uniformly distributed [26]. The heat generation within the battery, as described in [27] and [28], primarily includes two components. First, the irreversible heat is generated by the battery resistance, including ohmic resistance $\dot{Q}_o$ and polarization resistance $\dot{Q}_{\mathrm{po}}$. Second, the reversible heat $\dot{Q}_r$ is generated by the entropy change resulting from the deintercalation and intercalation of lithium ions in the anode and cathode. Therefore, heat generation can be expressed as follows [29]:

$$\begin{aligned} \dot{Q}_c &= \dot{Q}_o + \dot{Q}_{\mathrm{po}} + \dot{Q}_r \\ \dot{Q}_o &= I_c^2 R_o \\ \dot{Q}_{\mathrm{po}} &= I_{s1}^2 R_s + I_{l1}^2 R_l \\ \dot{Q}_r &= I_c T_c \cdot \frac{\partial V_{OCV,c}}{\partial T_c} \end{aligned} \tag{4}$$

where $\dot{Q}_c$ denotes the heat generation by a single battery cell, T_c is the battery cell temperature, and $\partial V_{OCV,c}/\partial T_c$ is the temperature rise coefficient of electromotive force [6].

2) OCV and Entropy Coefficient: To characterize the temperature rise coefficient of electromotive force, the OCV test was conducted under different temperature conditions at 25 °C and 40 °C for different SOCs. The measurement result is shown in Fig. 3. The entropy coefficient is defined as follows [30]:

$$\frac{\partial V_{OCV,c}}{\partial T_c}(\mathrm{SOC}_c) = \frac{V_{OCV,T1} - V_{OCV,T2}}{T_1 - T_2} \tag{5}$$

where $V_{OCV,Tx}$ is the cell OCV measured at a certain cell temperature T. $\partial V_{OCV,c}/\partial T_c$ can be summarized as a function of SOC by polynomial fitting. Taking discharging as an example, the fitting expression is shown as (6). The detailed expression of $d_{i,dis}$ is shown in supplementary material (2.7)

$$\frac{\partial V_{OCV,dis}}{\partial T} = \sum_{i=1}^{7} d_{i,dis} \mathrm{SOC}_c^{i-1}. \tag{6}$$

C. Aging Model

Battery aging is an important battery research area because it limits the power and energy capacity of the battery. Empirical and semi-empirical aging models are commonly employed due to their simplicity [31]. This study proposes

an empirical aging model for the Samsung INR18650-35E battery cell based on the public cycling dataset from [32]. This dataset includes various cycling scenarios, considering different cycling temperatures (25 °C, 35 °C, and 45 °C) and charging C-rates (0.25C, 0.5C, and 1C) while maintaining a discharge rate of 1C.

The proposed empirical aging model is shown in (7) and is composed of three distinct parts to model each of three battery aging stress factors, namely, throughput (Ah), C-rate (I_{rate}), and cell temperature (T_{c}). A polynomial equation is utilized in this study to model the effect of throughput on battery degradation. The validity of this choice is supported in Fig. 2.3 in the supplementary material.

Concerning temperature dependency, it is common to employ the Arrhenius law or similar exponential relationships. Additionally, polynomial relations can be utilized to model the pre-exponential factors. In the context of C-rate, an exponential increase in capacity losses to C-rate is typically used, often combined with the Arrhenius-like equation [31], [33]. Thus, the function form of the empirical cycle life model is given by (7) and (8)

$$Q_{\text{loss},\%} = A_1(T_{\text{c}}) \cdot \exp[A_2(T_{\text{c}}) \cdot B_1(I_{\text{rate}})] \cdot C_1(Ah) \tag{7}$$

$$A_1(T) = a_1 T_{\text{c}}^2 + a_2 T_{\text{c}} + a_3$$

$$A_2(T) = -\frac{E_a}{R_g T_{\text{c}}}$$

$$B_1(I_{\text{rate}}) = b_1 I_{\text{rate}}^2 + b_2 I_{\text{rate}} + b_3$$

$$C_1(Ah) = c_1 Ah^3 + c_2 Ah^2 + c_3 Ah + c_4 \tag{8}$$

$$\text{SOH}_n = \text{SOH}_0 - \frac{Q_{\text{loss},\%}}{100} \tag{9}$$

where $Q_{\text{loss},\%}$ represents the percentage of capacity loss, T_{c} denotes the battery temperature in kelvin (K), I_{rate} is the C-rate, and Ah stands for the cumulative throughput of the battery cell. E_a is the activation energy, which equals 31 500 J mol^{-1}, and R_g is the universal gas constant 8.314 J K^{-1} mol^{-1} [34]. SOH_0 is the initial SOH of the battery cell, which is 1 for a fresh cell. SOH_n is the cell SOH after n cycles. Based on the dataset, the fit results are summarized in supplementary material Table III.

With the empirical model (7) and (8), the capacity fade under different temperatures and rates throughout cycling can be predicted. In Fig. 4, the predicted capacity fade is compared to the experimentally measured capacity loss from the dataset for all C-rates at each temperature. The cycling conditions are denoted as X-Y/Z, where X is the temperature and Y/Z represents the charge/discharge current rate. The red diagonal line indicates the 45° line, indicating where the predicted losses align with the actual losses measured experimentally. The existing empirical model exhibited an RMSE of 1.31, an MAE of 1.11, and a coefficient of determination (R^2) of 0.9386, with a maximum deviation of 4 observed between the predicted and measured capacity loss in percentage.

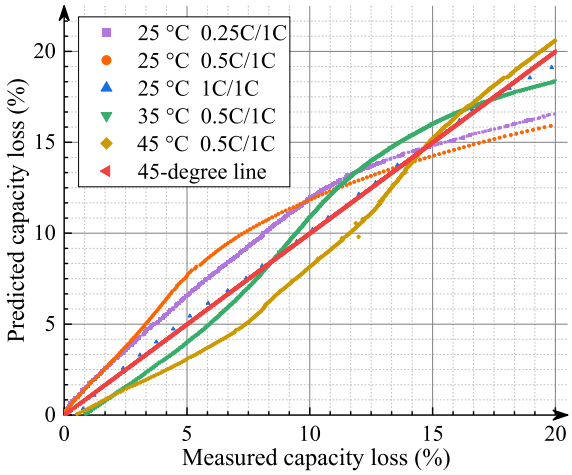

Fig. 4. Results of battery capacity prediction.

III. Battery Pack Design and Model

A. BTMS Design

BTMS can be classified into four main categories based on the cooling medium: air cooling, liquid cooling, phase change material cooling, and heat pipe cooling [35]. For AEA applications, air cooling offers unique advantages such as simplicity, cost-effectiveness, direct utilization of ambient low-temperature and high-speed airflow, and lightweight design [36]. However, the air-cooling system is less effective during ground operations, takeoff, go-around, and other phases characterized by high power demand and low airspeed [37]. In contrast, high-speed climb, descent, and cruise phases can result in excessive airflow, potentially overcooling the battery. Besides, the battery is exposed to abrupt temperature changes during climbs and descents due to the rapid altitude change [38], [39]. Additionally, directing airflow to battery packs distributed along the wings requires extra ducting, which may negatively affect the aircraft's aerodynamic performance. Therefore, in this study, liquid cooling is selected as a highly efficient method due to the high thermal conductivity and specific heat capacity of liquids. Additionally, liquid-cooling systems have a compact structure, occupying less volume and allowing placement in tighter spaces. These attributes make liquid cooling a highly practical and preferable choice for near-term short-range small AEA applications, offering a high heat transfer coefficient and minimal parasitic power consumption compared to other cooling strategies [14], [18], [35].

Regarding the cell shape formats, three Li-ion cell formats are cylindrical, pouch, and prismatic. The prismatic and pouch design offers improved packing efficiency, while cylindrical cells show better safety, cost, and structural integrity [40]. Notably, the first commercially available AEA, the two-seater Pipistrel Velis Electro, is powered by two liquid-cooled battery packs made of cylindrical cells [41]. Consequently, cylindrical batteries are selected for the AEA battery pack in this study, combined with indirect liquid cooling using water as the coolant due to its high specific heat capacity, excellent thermal conductivity, and low viscosity [35].

The BTMS employs a wavy flat tube as the cooling channel to enhance heat transfer between the batteries and the cooling plate, as illustrated in Fig. 5. In this configuration, the walls of the cooling channel make direct contact with the surfaces of the cylindrical cells. This is the most well-known liquid-cooling system, increasing the heat exchange area between the battery cell and coolant and ensuring effective

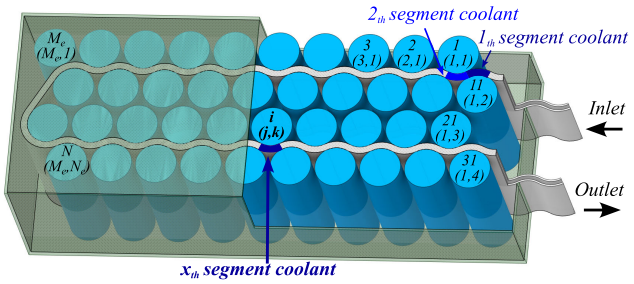

Fig. 5. Indirect liquid-cooling BTMS with a wavy flat tube.

temperature control and uniformity [42]. For the complete cooling loop, it consists of a heat exchanger system, a reservoir tank, a pump, heating elements to heat up the coolant under high-altitude low-ambient-temperature conditions, regulating valves, fans, and piping for coolant circulation. The heat exchanger system operates in a dual-inlet configuration, allowing control over the amount of air entering the system. During high airspeed operation, the ram air inlet is controlled via regulating valves to maintain optimal thermal performance. In low airspeed conditions, the fan is turned on to ensure sufficient airflow through the heat exchanger system [43].

B. Electrical Submodel

A battery pack comprises multiple modules, each consisting of series/parallel combinations of individual cells. Cells are connected in parallel to meet high energy or power capacity demands, while series connections are utilized to achieve the desired system voltage. Commonly used electrical configurations include SCM and PCM. In the SCM topology, M_e cells are connected in series to form an SCM, and then, N_e SCMs are connected in parallel to assemble the battery pack. In the PCM topology, N_e cells are connected in parallel to create a PCM, with M_e such modules connected in series to construct the battery pack. Schematics of commonly used electrical configurations are shown in supplementary material Fig. 3.1.

For the electrical arrangement of the cell within the battery pack, a coordinate index pair $(j,k) \in (\mathcal{J} \times \mathcal{K})$ is used to denote the battery cell index, where $\times$ is the Cartesian product, $\mathcal{J} = \{1 \le j \le M_e\}$, and $\mathcal{K} = \{1 \le k \le N_e\}$. The location of each cell within the battery pack is denoted by an index number $i \in \mathcal{I} = \{1 \le i \le N\}$, where $N = N_e M_e$ represents the total number of cells in the pack [11]. Thus, the electrical submodel comprises $N + 1$ elements. N electrical elements are employed to predict the voltages, currents, and SOCs of each battery cell in response to input sources. One electrical interconnection element is utilized to estimate the distribution of input current or voltage among the cells.

1) Electrical Elements: The second-order RC Thévenin-based model, depicted in Fig. 2, is employed to model each cell within the battery pack. Depending on the type of input source, (1) or (2) together with (3) is used to express the electrical response of each cell. To model manufacturing variability, the internal ohmic resistance R_o and full capacity S_f parameters within each cell are assumed to conform to a normal distribution [44]. Consequently, for a specific cell coordinate index pair (j, k), the parameters are varied according to the following equations:

$$R_{o,(j,k)} = R_o \cdot r_{R,(j,k)} \tag{10}$$

$$S_{f,(j,k)} = S_f \cdot r_{S,(j,k)} \tag{11}$$

where R_o and S_f are the base internal ohmic resistance and full capacity, respectively. $r_{R,(j,k)} \sim \mathcal{N}(1, \sigma_R)$ and $r_{S,(j,k)} \sim \mathcal{N}(1, \sigma_S)$ are normally distributed numbers. The internal resistance and full capacity standard deviations are denoted as σ_R and σ_S, respectively. The resulting varied parameters are represented as $R_{o,(j,k)}$ and $S_{f,(j,k)}$. For simplicity, throughout the remaining discussion, we assume that σ_R and σ_S are equal and set to 0.025 [11].

2) Electrical Interconnection Element: The input current for a cell with index i and index pair (j,k), denoted as $I_{i,(j,k)}$, is calculated using Kirchhoff's voltage and current laws. Depending on the input source type, $I_{i,(j,k)}$ is determined based on the input current or voltage of the battery pack. First, when the input is a current source, the electrical interconnection element is represented by the following set of linear equations:

$$\mathbf{A} \cdot \mathbf{I_c} = \mathbf{B} \cdot [\mathbf{OCV} + \mathbf{V_s} + \mathbf{V_I}] + \mathbf{C} \cdot I_{\mathrm{p}} \tag{12}$$

where I_{p} represents the input current of the battery pack. The vectors $\mathbf{OCV(t)} \in (\mathbb{R}^N \times 1)$, $\mathbf{V_s(t)} \in (\mathbb{R}^N \times 1)$, and $\mathbf{V_I(t)} \in (\mathbb{R}^N \times 1)$ denote the OCV, the voltage across the short-time transient RC pair, and the voltage across the long-term transient RC pair, respectively, of each cell at time instant t. The vector $\mathbf{I_c(t)} \in (\mathbb{R}^N \times 1)$ represents the current of each battery cell at time instant t. Detailed expressions for these variables can be found in supplementary material (3.1)–(3.4). The electrical interconnection element parameters consist of matrices: $\mathbf{A} \in (\mathbb{R}^N \times \mathbb{R}^N)$, $\mathbf{B} \in (\mathbb{R}^N \times \mathbb{R}^N)$, and $\mathbf{C} \in (\mathbb{R}^N \times 1)$. The entries of these matrices depend on the pack topology and cell index. For the SCM topology, the corresponding matrices are provided in the supplementary material as (3.5)–(3.7). Similarly, for the PCM topology, the matrices are presented in the supplementary material as (3.8)–(3.10). Equation (13) is used for matrix indexing

$$f(j,k) = (k-1) \times M_e + j. \tag{13}$$

When the input is a voltage source, the electrical relationship within a single string in the SCM topology can be expressed using (14). This equation specifically captures the interplay of variables within one string so that the cell index $i \in \{(k-1)M_e + 1 \le i \le kM_e\}$. However, when considering the electrical current of the entire battery pack, which consists of multiple strings, this equation needs to be solved iteratively for each individual string

$$\mathbf{S} \cdot \mathbf{I_{vs}} = \mathbf{D_s}. \tag{14}$$

The current vector $\mathbf{I_{vs}} \in (\mathbb{R}^{3M_e} \times 1)$ represents the currents flowing through the resistors of the two RC pairs and the cell current within a single string. The detailed expressions of the current vector can be found in supplementary material (3.11). The electrical interconnection element parameters, including $\mathbf{S} \in (\mathbb{R}^{3M_e} \times \mathbb{R}^{3M_e})$ and $\mathbf{D_s} \in (\mathbb{R}^{3M_e} \times 1)$, are defined and described in supplementary material (3.12) and (3.13).

For the pack topology PCM, the electrical relationship inside a battery pack can be expressed using the following equation:

$$\mathbf{P} \cdot \mathbf{I_{vp}} = \mathbf{D_p}. \tag{15}$$

The current vector $\mathbf{I}_{\text{vp}} \in (\mathbb{R}^{3N} \times 1)$ represents the currents flowing through the resistors of the two RC pairs and the cell current in the whole pack. The detailed expressions of the current vector can be found in supplementary material (3.14). The electrical interconnection element parameters, including $\mathbf{P} \in (\mathbb{R}^{3N} \times \mathbb{R}^{3N})$ and $\mathbf{D_p} \in (\mathbb{R}^{3N} \times 1)$, are defined and described in supplementary material (3.15) and (3.16).

C. Thermal Submodel: Indirect Liquid Cooling

1) Battery: Assuming adiabatic boundary conditions on the top and bottom surfaces of the battery pack, the domain can be simplified to a 2-D model [45]. Therefore, to capture the transient thermal behavior of each battery cell within the battery pack during operation, a 2-D lumped model is employed with acceptable accuracy and low computational complexity. Direct conduction heat transfer between adjacent battery cells is not considered since they are not in direct contact. The heat generated by the battery during operation is transferred to the flowing coolant and the surrounding air. Therefore, the energy governing equation in the following equation is derived based on [46]:

$$m_{\text{c}} C_{\text{p,c}} \frac{dT_{\text{c,i}}}{dt} = \dot{Q}_{\text{c,i}} - \dot{Q}_{\text{c-cl,i}} - \dot{Q}_{\text{c-ext,i}} \tag{16}$$

where m_{c} is the battery cell mass, $C_{\text{p,c}}$ is the battery specific heat capacity at constant pressure, i is the battery cell index with the coordinate index pair (j, k), which is introduced in Section III-B. $T_{\text{c,i}}$ is the ith battery cell temperature. $\dot{Q}_{\text{c,i}}$ represents the heat generation rate of the ith battery cell and $\dot{Q}_{\text{c-cl,i}}$ denotes the heat transfer rate between the battery cell i and flowing coolant via the aluminum cooling channel wall, as represented by (17). $\dot{Q}_{\text{c-ext,i}}$ denotes the heat transfer rate between the battery cell i and exterior ambient air via battery pack encapsulation, as given by (19).

The liquid coolant dissipates the heat generated from the battery through the aluminum cooling channel wall. The entire coolant flow varies in temperature based on its position within the pack. Consequently, the coolant flow path is segmented into N sections, each corresponding to one battery, as shown in Fig. 5. The coolant segment is indexed by x, which increments sequentially, starting from $x = 1$ at the inlet and ending at $x = N$ at the outlet

$$\dot{Q}_{\text{c-cl,i}} = \frac{1}{\frac{L_{\text{Al}}}{k_{\text{Al}}} + \frac{1}{h_{\text{Al-cl,i}}}} S_{\text{c-cl}} \Delta T_{\text{c,i}} \tag{17}$$

where k_{Al} represents the thermal conductivity of aluminum, L_{Al} is the thickness of the aluminum wall, $h_{\text{Al-cl,i}}$ stands for the forced convection coefficient, $S_{\text{c-cl}}$ denotes the conducting area between the individual battery cell and the cooling channel wall, and $\Delta T_{\text{c,i}}$ is the temperature difference between the ith battery cell and the coolant flow in the xth cooling channel segment.

Upon calculation, the Reynolds number in this study always does not exceed the order of hundreds. The viscous forces significantly outweigh the inertial forces, resulting in a stable, laminar flow. For $h_{\text{Al-cl,i}}$, as the flow is laminar, it can be determined using the following equation [12]:

$$h_{\text{Al-cl,i}} = \text{Nu} \cdot \frac{k_{\text{cl}}}{D_{\text{cl}}}$$
$$\text{Nu} = 1.86 \cdot (\text{RePr})^{1/3} \left(\frac{D_{\text{cl}}}{L_{\text{cl}}}\right)^{1/3} \left(\frac{\mu_{\text{cl}}}{\mu_{\text{Al,cl}}}\right)^{0.14} \tag{18}$$

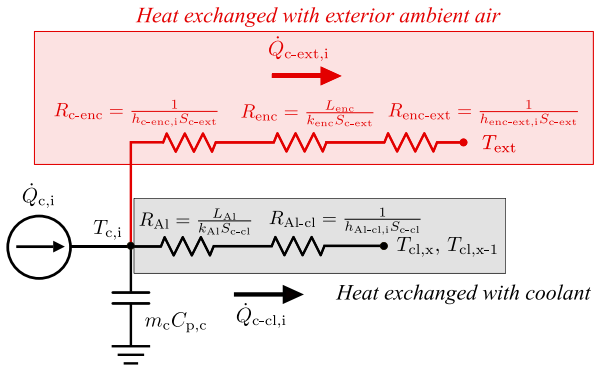

Fig. 6. Thermal resistance network for the liquid-cooled battery pack.

where Pr is the Prandtle number; Re is the Reynolds number; L_{cl} is the cooling channel length; μ_{cl} is the viscosity at coolant temperature; $\mu_{\text{Al,cl}}$ is the viscosity at wall temperature; k_{cl} is the coolant thermal conductivity; and D_{cl} is the characteristic length of the flow, which is the equivalent diameter of the channel.

The battery pack is assumed to be installed within the wing of the AEA [47], with the ambient temperature of the battery pack considered equal to the external ambient temperature. This assumption is based on the aluminum wing material of the Cessna 172, which has high thermal conductivity. Additionally, the wing's surface is subject to forced convection with turbulent airflow, characterized by a high heat transfer coefficient [48], [49]. Thus, heat dissipation of the battery occurs not only through the coolant but also via the external cold air at high altitudes through the battery pack encapsulation material, as illustrated in the red line in Fig. 6. In this design, aerogel is selected as the encapsulation material for the packaging due to its excellent thermal insulation properties, which help insulate the battery pack thermally from the cold ambient conditions encountered at high altitudes, thereby reducing heat loss to the environment [50]. Additionally, as one of the lightest solid materials, it can minimize the weight of the packaging [51].

Hence, the heat transfer rate between the battery cell and exterior ambient air is represented by the following equation:

$$\dot{Q}_{\text{c-ext,i}} = \frac{1}{\frac{1}{h_{\text{c-enc,i}}} + \frac{L_{\text{enc}}}{k_{\text{enc}}} + \frac{1}{h_{\text{enc-ext,i}}}} S_{\text{c-ext}} \left(T_{\text{c,i}} - T_{\text{ext}}\right) \tag{19}$$

where k_{enc} and L_{enc} represent the thermal conductivity and thickness of encapsulation material, respectively; $h_{\text{c-enc,i}}$ stands for the natural convection coefficient between battery and encapsulation; $h_{\text{enc-ext,i}}$ stands for the natural convection coefficient between encapsulation and surrounding air; $S_{\text{c-ext}}$ denotes the contact area between the individual battery cell and pack encapsulation wall; and T_{ext} denotes the external air temperature, which varies with altitude throughout the flight.

2) Liquid Coolant: Water: Within each liquid coolant segment, uniform mass flow rates are assumed [12]. Since the coolant temperature in each segment differs between the inlet and outlet, the logarithmic averaged temperature difference model is employed to characterize the temperature difference [52]

$$\Delta T_{\text{c,i}} = \frac{T_{\text{cl},x} - T_{\text{cl},x-1}}{\ln\left(\frac{T_{\text{c,i}} - T_{\text{cl},x-1}}{T_{\text{c,i}} - T_{\text{cl},x}}\right)} \tag{20}$$

where $T_{\mathrm{cl},x-1}$ is the inlet temperature of the xth segment of the coolant and $T_{\mathrm{cl},x}$ is the outlet temperature of the xth segment of the coolant.

The heat transferred into the coolant, $\dot{Q}_{\mathrm{c-cl,i}}$, causes a temperature difference between the inlet and the outlet. Therefore, the energy governing equation for each coolant segment is expressed as (21) [11], [12], [43]. The outlet temperature of the previous segment is the inlet temperature of the next segment. The relationship between i and x is provided in the supplementary material as (3.17)

$$\rho_{\mathrm{cl}} A_{\mathrm{cl}} U_{\mathrm{cl}} C_{\mathrm{p,cl}} \left(T_{\mathrm{cl},x} - T_{\mathrm{cl},x-1}\right) = \dot{Q}_{\mathrm{c-cl,i}} \tag{21}$$

where ρ_{cl} is the density of the liquid coolant, A_{cl} is the cross section of wavy tubes, U_{cl} is the liquid coolant velocity, and $C_{\mathrm{p,cl}}$ is the heat capacity of the liquid coolant.

The entire pack model was constructed using MATLAB and PyCharm software. The block diagram illustrating the computational process is depicted in supplementary material Fig. 3.2.

IV. Optimization of BTMS for Electric Aircraft Operation

A. Physical Model

The battery pack in this study is designed by connecting multiple battery modules, offering greater modularity compared to cell-level designs. This modular approach provides several advantages. When the AEA undergoes maintenance on the ground, the modular design facilitates easier and more efficient servicing. During flight, modularity enables independent control of each battery module, minimizing the risk of a complete battery pack shutdown in case of a failure in one or more cells. Furthermore, sufficient thermal independence between modules reduces heat transfer among them, simplifying the thermal behavior of the battery pack and alleviating the burden on the BTMS. Therefore, the following discussion will first focus on the battery at the module level.

The battery module comprises 40 INR18650-35E batteries arranged in four rows, as shown in Fig. 5. The connectors and fixtures between the batteries have a negligible effect on heat transfer [42]. For the electrical arrangement, the PCM topology is adopted, with $M_e = 10$ and $N_e = 4$. The cell and coolant indices within the battery module are depicted in Fig. 5. The properties of each material used in the battery module are listed in supplementary material Table IV.

B. Cell-Level Model Verification

An experiment was conducted to verify the proposed battery electrothermal model at the cell level. Fig. 7 illustrates the experimental setup, which comprises a battery tester (16 channels, each rated for 25 V and 10 A), a temperature chamber to regulate ambient temperature, a K-type thermocouple ($\pm[0.5\% + 0.5\,^{\circ}\mathrm{C}]$) to measure battery cell surface temperature, and a host PC for monitoring, controlling the test, and recording data.

A typical flight profile for a small aircraft consists of five distinct phases: takeoff, climb, cruise, descent, and landing. In this study, only the first four phases are considered, as the landing phase involves minimal energy consumption, lower power demand, and negligible BTMS requirements. Hence,

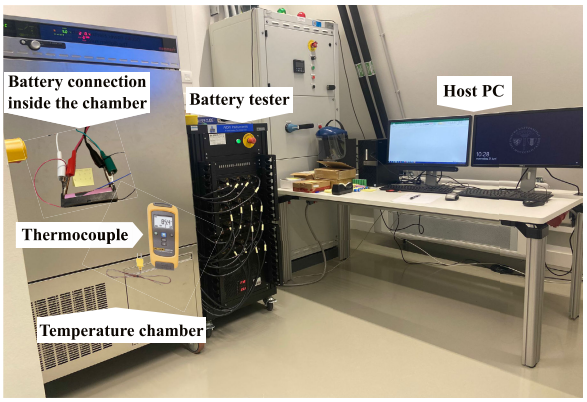

Fig. 7. Experimental setup for cell-level battery tests.

an example four-seater AEA power profile, including takeoff, climb, cruise, and descent, as shown in supplementary material Fig. 4.1(a), was normalized to the cell level and applied to the battery cell. The specifications of the example AEA (range 130 km), specifically a retrofitted Cessna 172R, are provided in supplementary material Table V. The detailed design of the retrofit AEA and the estimation of the power profile can be found in [24]. The temperature chamber was set to 25 °C. The resulting simulated and experimental voltage–current and temperature data are shown in Fig. 8. For temperature prediction, the electrothermal battery cell model achieved an MAE of 0.30, an RMSE of 0.24, and a coefficient of determination (R^2) of 0.9940, demonstrating its high accuracy and reliability.

C. Module-Level Model Verification

To validate the thermal model presented in Section III, numerical simulations of the battery module under an AEA flight mission are performed using the commercial CFD software ANSYS FLUENT. Since the Reynolds number of the flow within the channel does not exceed 2300, the flow is modeled as laminar. Boundary conditions are defined with a mass flow inlet and a pressure outlet for the coolant. The initial temperatures of the coolant, battery cells, inner air, and outer wall temperature are set to 25 °C. The heat generation from the battery cells is defined using a user-defined function and calculated based on the analytical cell and pack models presented in Sections II and III. The user-defined function updates the heat generation rate at each time step based on the cell temperature and the module power. The module's power profile is derived from the same AEA power profile as in Section IV-B. The ambient temperature changes with the altitude, as shown in supplementary material Fig. 4.1(b).

To ensure the accuracy and reliability of the numerical simulation, a mesh independence verification was conducted using various mesh numbers. As shown in Fig. 9, the maximum cell temperature for mesh quantities ranging from 1.2×10^4 to 2.2×10^5 elements was evaluated. The results indicate that increasing the mesh quantity does not significantly change the temperature trends, which remain consistent across different mesh sizes. Quantitatively, the difference in maximum cell temperature between the 1.16×10^5 and 2.19×10^5 element meshes is less than 0.4%, confirming that the solution has effectively converged. Therefore, a mesh size of

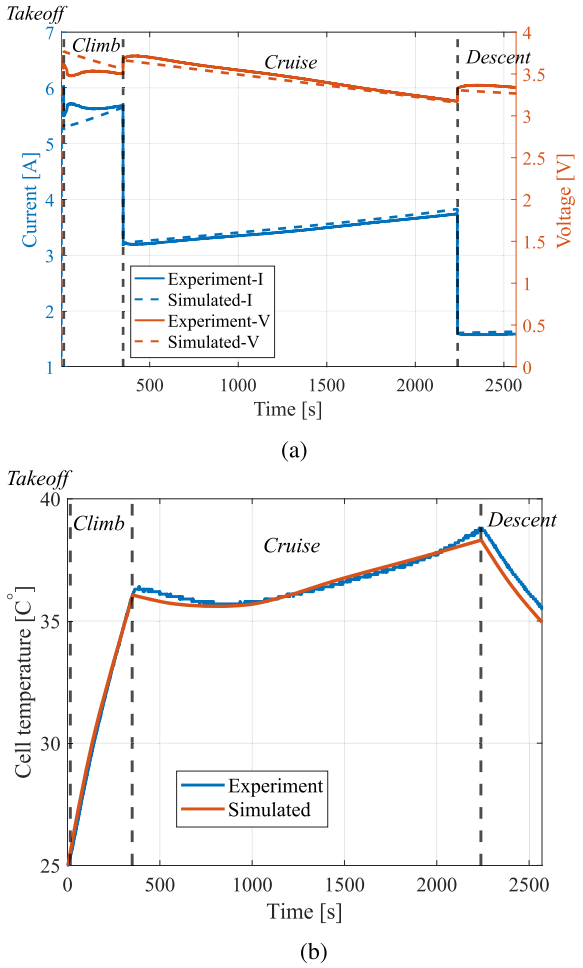

Fig. 8. Experimental verification under specified AEA power profile. (a) Voltage and current profile. (b) Temperature profile.

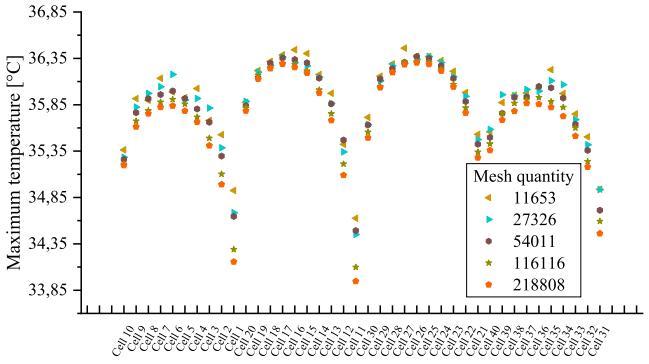

Fig. 9. Maximum cell temperature comparison with different mesh quantities.

1.16×10^5 elements was selected for all subsequent simulations to balance accuracy and computational efficiency.

The solver time step can influence the results in the numerical simulation process. Therefore, a time step independence study was conducted using time steps of 1, 2, and 3 s. The results of this verification are shown in Fig. 10. It can be observed that the maximum cell temperature of the battery pack remains consistently as the time step increases, indicating good numerical stability. A time step of 1 s is selected

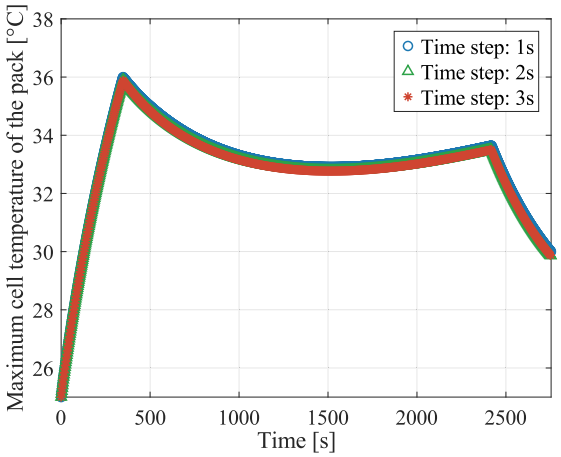

Fig. 10. Maximum cell temperature of the battery pack with different time steps.

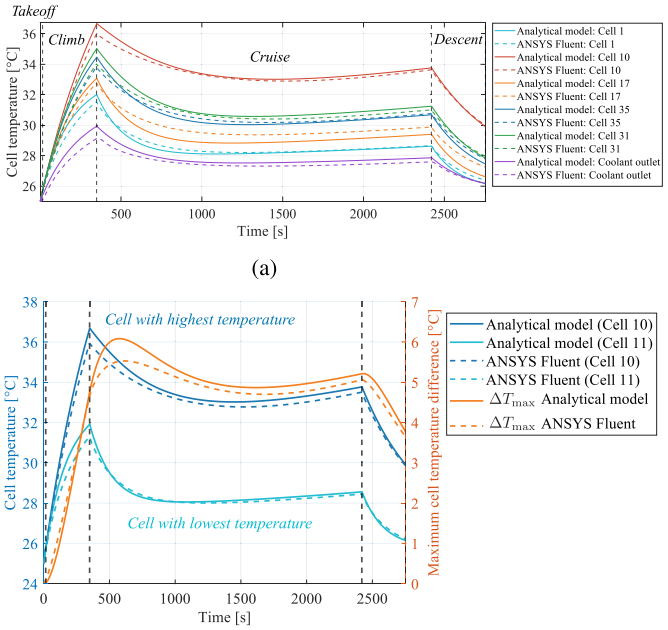

Fig. 11. Comparison of the analytical model and simulation for the base case. (a) Different cell temperatures. (b) Maximum temperature difference between cells.

for subsequent simulations to maintain consistency with the temporal resolution of the analytical model.

The base case, defined as $[L_{\mathrm{Al}}, W_{\mathrm{cl}}, D_{\mathrm{cell}}, L_{\mathrm{enc}}] = [1.0, 2.4, 24, 2]$ mm, is simulated. These parameters represent the thickness of the aluminum coolant channel wall (L_{Al}), the width of the coolant inlet (W_{cl}), the distance between cell centers (D_{cell}), and the aerogel package wall thickness (L_{enc}). The gravimetric and volumetric energy densities of the battery module, including the BTMS, are 208.48 W h kg^{-1} and 292.43 W h L^{-1}, respectively. A comparison between the results predicted by the analytical model in Section III and those obtained from ANSYS Fluent is shown in Fig. 11. The maximum error in cell temperature prediction between the model output and CFD simulation temperature occurs in cell 14 (0.87 °C), reaching 3.1% at approximately 700 s. The average MAE, RMSE, and MAPE for the entire battery pack

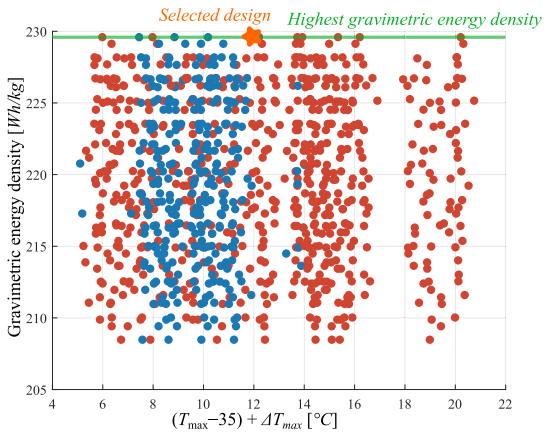

(a)

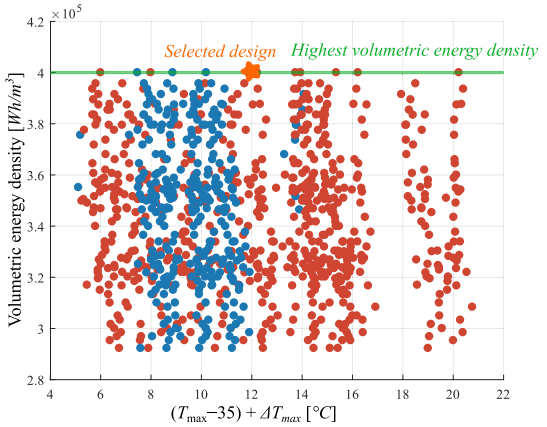

(b)

Fig. 12. Iteration results for different geometric parameters (red indicating pre-eliminated designs due to poor thermal performance and blue indicating feasible designs). (a) Gravimetric energy density versus thermal performance. (b) Volumetric energy density versus thermal performance.

are 0.31%, 0.36%, and 1.02%, respectively, demonstrating excellent accuracy overall. The coolant outlet temperature prediction also shows strong agreement, with an MAE of 0.28, an RMSE of 0.3308, and an MAPE of 1.01%.

To further demonstrate the robustness of the model, additional simulations were conducted with initial ground temperatures set to 0 °C and 40 °C. For the case with an initial ground temperature of 0 °C, the MAE, RMSE, and MAPE for the entire battery pack were 0.33%, 0.38%, and 1.10%, respectively. Under the 40 °C condition, these values increased slightly to 0.48%, 0.50%, and 1.59% while still indicating a high level of accuracy.

D. Optimization of the BTMS

1) Geometric Configurations and Coolant Flow Parameters: To optimize the thermal performance and energy density of the battery pack, geometric and coolant flow parameters are iterated based on the module power profile from the example AEA. These parameters include aluminum wall thickness L_{Al}, coolant inlet width W_{cl}, cell-to-cell distance D_{cell}, aerogel wall thickness L_{enc}, coolant inlet velocity $U_{\mathrm{cl,in}}$, and coolant inlet temperature $T_{\mathrm{cl,in}}$. The iteration values for these parameters are

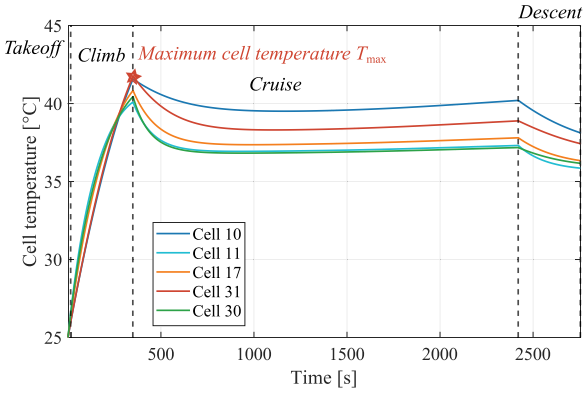

Fig. 13. Different cell temperatures for the optimal case.

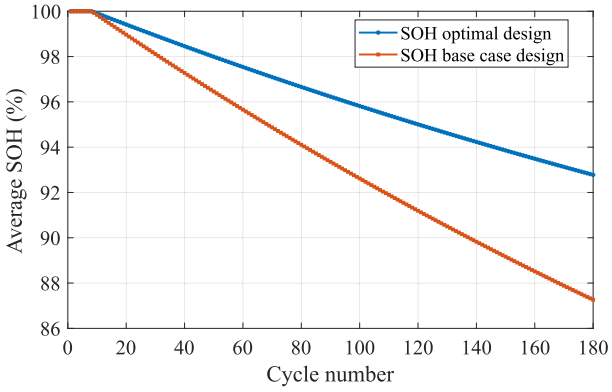

Fig. 14. SOH over 180 cycles of both designs.

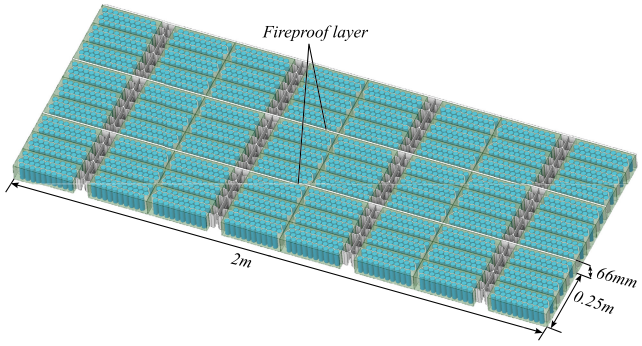

Fig. 15. Geometry of three battery packs.

provided in the following equation:

$$\begin{aligned} L_{\mathrm{Al}} &= [0.4\,,\ 0.7\,,\ 1.0]\,\mathrm{mm} \\ W_{\mathrm{cl}} &= [1.6\,,\ 2.0\,,\ 2.4]\,\mathrm{mm} \\ D_{\mathrm{cell}} &= [20\,,\ 22\,,\ 24]\,\mathrm{mm} \\ L_{\mathrm{enc}} &= [0.5\,,\ 1\,,\ 2]\,\mathrm{mm} \\ U_{\mathrm{cl,in}} &= [0.01\,,\ 0.02\,,\ 0.03]\,\mathrm{m\,s^{-1}} \\ T_{\mathrm{cl,in}} &= [25\,,\ 30\,,\ 35\,,\ 40]\,^{\circ}\mathrm{C}. \end{aligned} \tag{22}$$

The proposed ETA battery cell and pack model described in Sections II and III then computes the thermal performance over the entire flight mission profile of the aircraft and evaluates the energy density. The initial temperature of the whole battery module is set to be 25 °C. Iteration results for

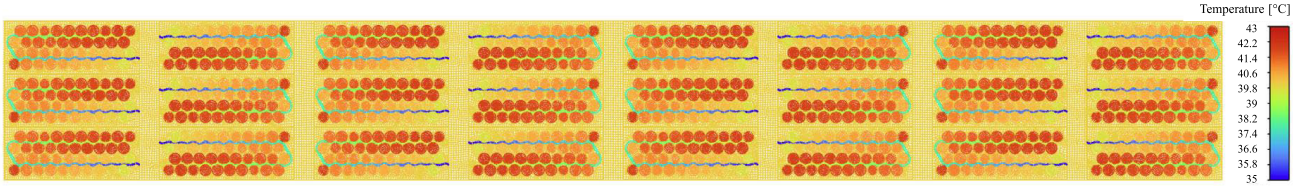

Fig. 16. Temperature contour of the battery pack at 350 s.

different geometric configurations and coolant flow parameters are shown in Fig. 12. The volumetric energy density varies significantly as these geometric parameters affect the total volume a lot, especially the cell spacing. While $\Delta T_{\max}$ represents the maximum temperature difference between cells and $T_{\max}$ is defined as the maximum cell temperature among the whole battery pack, the sum of these two metrics is used as the criterion to evaluate the thermal performance. This criterion reflects both temperature uniformity and the maximum temperature.

As shown in Fig. 2.3, the high-energy-density 35E cell demonstrates better lifetime performance at 35 °C–45 °C compared to 25 °C. Therefore, designs with $T_{\max}$ exceeding 45 °C, below 35 °C, or with $\Delta T_{\max}$ greater than 5 °C are pre-eliminated due to their relatively poor thermal performance. These designs are colored in red in Fig. 12, while the remaining feasible designs are shown in blue.

According to the iteration results, the highest gravimetric (229.59 W h kg^{-1}) and volumetric energy densities (400.16 W h L^{-1}) are achieved with $[L_{\text{Al}}, W_{\text{cl}}, D_{\text{cell}}, L_{\text{enc}}] = [0.4, 1.6, 20, 0.5]$ mm. Among the designs that achieve maximum energy densities, four combinations of coolant inlet temperature and velocity remain: $C_1 = [0.03\,\text{m s}^{-1}, 30\,°\text{C}]$, $C_2 = [0.02\,\text{m s}^{-1}, 25\,°\text{C}]$, $C_3 = [0.02\,\text{m s}^{-1}, 35\,°\text{C}]$, and $C_4 = [0.03\,\text{m s}^{-1}, 35\,°\text{C}]$. Among them, C_1 and C_2 are excluded due to lower average pack temperatures (less than 35 °C). For the remaining cases, C_3 and C_4, the corresponding $T_{\max}$, $\Delta T_{\max}$, and the average battery pack temperature T_{avg} values are [42.50 °C, 4.46 °C, and 37.41 °C], and [41.51 °C, 3.67 °C, and 36.74 °C], respectively. Since the thermal performance of C_3 and C_4 is similar, C_3 is selected due to lower pumping power consumption and relatively good thermal performance.

2) Variable Inlet Velocity: To further improve the temperature uniformity, the inlet velocity is increased during the cruise phase, as this phase exhibits the highest temperature difference. The inlet velocity is varied between $U_{\text{cl,in}} = [0.02, 0.035, 0.05, 0.075]\,\text{m s}^{-1}$. By increasing the velocity, $\Delta T_{\max}$'s are reduced to $\Delta T_{\max} = [4.46, 3.44, 3.11, 3.10]\,°\text{C}$. Since further increasing the velocity shows insignificant improvement in thermal performance, the inlet velocity is set to 0.05 m s^{-1} during the cruise phase and 0.02 m s^{-1} during the takeoff, climb, and descent phases.

For the optimal case, the cell temperatures throughout the entire flight mission are shown in Fig. 13. The maximum temperature ($T_{\max}$) occurs at 350 s for cell 31, reaching 41.76 °C at the end of the climb phase. The maximum temperature difference ($\Delta T_{\max}$) is 3.11 °C, observed between cells 10 and 30 at 556 s, which corresponds to the start of the cruise phase. The average temperature throughout the entire flight mission is 37.49 °C.

In addition to thermal performance, the cyclic aging performance is compared between the optimal and base cases. Using 0.5C CCCV charging, 180 cycles are simulated for both designs under the AEA power profile, to represent one flight per day over six months. After 180 cycles, the average SOH of the optimal design pack is 92.78%, as shown in Fig. 14. Compared to 87.26% for the base design, the optimal design demonstrates improved lifetime performance (5.51%), due to its superior temperature uniformity and higher cell average temperature.

E. Module-to-Pack Structure

A battery pack consists of multiple battery modules. Considering the BMS capability, each pack contains 24 modules, arranged in eight rows and three columns. As shown in Fig. 15, the connection between battery modules within a single battery pack is modularized. The pack comprises repeated structural units, with the smallest repeated unit comprising two rows totaling six modules. The inlets and outlets of each module are interconnected and go through the aerogel fireproof layer between adjacent battery packs. This configuration shortens the total flow channel length, improving thermal management efficiency and reducing the BTMS weight.

The optimized dimensions of each battery module in Section IV-D are 83.9 × 221 × 66 mm. Taking into account the interconnection structures between modules, the overall dimensions of a single battery pack are designed as 0.25 × 2 × 66 mm. The proposed design achieves a gravimetric energy density of 227.01 W h kg^{-1} and a volumetric energy density of 353.67 W h L^{-1}. In comparison, the base design, using the same pack-level configuration, achieves 203.68 W h kg^{-1} and 263.32 W h L^{-1}. In total, 18 battery packs are arranged in a single-layer distribution within the aircraft wing.

The ANSYS simulation result at 350 s is presented in Fig. 16. It can be observed that the temperature distribution across all battery modules is nearly identical. This uniformity is attributed to the still air filling all gaps. The still air, in combination with the aerogel encapsulation, provides effective thermal insulation. These results confirm the effective thermal insulation capability of the battery module design and demonstrate the high scalability of the analytical model and the overall system architecture.

V. Conclusion

In this study, an optimal compact and lightweight liquid-cooled BTMS for small AEAs is proposed, based on an ETA battery pack model. This proposed pack model can predict the electrical, thermal, and aging dynamics of the battery pack under actual AEA operating conditions. Using

the proposed model, the effects of channel wall thickness (L_{Al}), coolant inlet width (W_{cl}), cell-to-cell interval (D_{cell}), aerogel package wall thickness (L_{enc}), inlet velocity ($U_{\mathrm{cl,in}}$), and inlet temperature ($T_{\mathrm{cl,in}}$) on the thermal performance and energy density are systematically analyzed. The structural parameters are optimized to minimize the weight and volume of the battery module, while the inlet coolant temperature and velocity are optimized to improve the thermal performance. After that, the module-to-pack structure is analyzed to evaluate scalability and system-level integration. Compared to the base case, the optimal design achieves an 11.45% increase in gravimetric energy density and a 34.31% increase in volumetric energy density at the pack level. Thermal performance is also improved, with a 2.91 °C decrease in the maximum cell temperature difference. The lifetime performance also demonstrates a 5.51% improvement in SOH after 180 cycles.

This modeling framework can be tailored to accommodate various thermal management designs, battery pack configurations, and operation conditions, allowing for fast yet detailed ETA simulations of large battery packs. Future work should focus on further refining the ETA model by extending it from 2-D to 3-D form, allowing for a more detailed representation of heat generation and temperature distribution within the battery cells, coolant flow profile, as well as heat transfer through the top and bottom surfaces of the battery pack, including the effects of electrical tab and connector structures. Furthermore, alternative battery thermal management strategies, such as hybrid cooling systems that combine liquid cooling with phase change materials, and the detailed design and analysis of the complete coolant loop considering the altitude effect, can be explored with a physical experimental setup in future studies.

REFERENCES

[1] Y. Liang, G. R. C. Mouli, and P. Bauer, "Charging technology for electric aircraft: State of the art, trends, and challenges," *IEEE Trans. Transport. Electrific.*, vol. 10, no. 3, pp. 6761–6788, Sep. 2024.

[2] S. S. Madani et al., "Exploring the aging dynamics of lithium-ion batteries for enhanced lifespan understanding," in *Proc. J. Phys., Conf.*, 2025, vol. 2968, no. 1, Art. no. 012017.

[3] E. Yousefi et al., "Liquid immersion cooling with enhanced Al_2O_3 nanofluid for large-format prismatic battery pack: Numerical and statistical investigation," *J. Thermal Anal. Calorimetry*, vol. 150, no. 5, pp. 3489–3507, Mar. 2025.

[4] M. Dubarry, N. Vuillaume, and B. Y. Liaw, "From single cell model to battery pack simulation for Li-ion batteries," *J. Power Sources*, vol. 186, no. 2, pp. 500–507, Jan. 2009.

[5] M. Dubarry, N. Vuillaume, and B. Y. Liaw, "Origins and accommodation of cell variations in Li-ion battery pack modeling," *Int. J. Energy Res.*, vol. 34, no. 2, pp. 216–231, Feb. 2010.

[6] Y. Li et al., "Optimization of charging strategy for lithium-ion battery packs based on complete battery pack model," *J. Energy Storage*, vol. 37, May 2021, Art. no. 102466.

[7] H.-K. Kim and K.-J. Lee, "Use of a multiphysics model to investigate the performance and degradation of lithium-ion battery packs with different electrical configurations," *Energy*, vol. 262, Jan. 2023, Art. no. 125424.

[8] M. Dubarry, G. Baure, C. Pastor-Fernández, T. F. Yu, W. D. Widanage, and J. Marco, "Battery energy storage system modeling: A combined comprehensive approach," *J. Energy Storage*, vol. 21, pp. 172–185, Feb. 2019.

[9] J. N. Lucero, V. A. Sujan, and S. Onori, "An experimentally validated electro-thermal EV battery pack model incorporating cycle-life aging and cell-to-cell variations," *IEEE Trans. Transport. Electrific.*, vol. 10, no. 4, pp. 8122–8136, Dec. 2024.

[10] S. M. Jordan, C. O. Schreiber, M. Parhizi, and K. Shah, "A new multiphysics modeling framework to simulate coupled electrochemical-thermal-electrical phenomena in Li-ion battery packs," *Appl. Energy*, vol. 360, Apr. 2024, Art. no. 122746.

[11] A. Cordoba-Arenas, S. Onori, and G. Rizzoni, "A control-oriented lithium-ion battery pack model for plug-in hybrid electric vehicle cycle-life studies and system design with consideration of health management," *J. Power Sources*, vol. 279, pp. 791–808, Apr. 2015.

[12] J. He, M. Sazzad Hosen, R. Youssef, T. Kalogiannis, J. Van Mierlo, and M. Berecibar, "A lumped electro-thermal model for a battery module with a novel hybrid cooling system," *Appl. Thermal Eng.*, vol. 221, Feb. 2023, Art. no. 119874.

[13] B. E. Lebrouhi, B. Lamrani, M. Ouassaid, M. Abd-Lefdil, M. Maaroufi, and T. Kousksou, "Low-cost numerical lumped modelling of lithium-ion battery pack with phase change material and liquid cooling thermal management system," *J. Energy Storage*, vol. 54, Oct. 2022, Art. no. 105293.

[14] H. Xu, X. Zhang, G. Xiang, and H. Li, "Optimization of liquid cooling and heat dissipation system of lithium-ion battery packs of automobile," *Case Stud. Thermal Eng.*, vol. 26, Aug. 2021, Art. no. 101012.

[15] Q. Liu et al., "Improved performance of Li-ion battery thermal management system by ternary hybrid nanofluid," *J. Energy Storage*, vol. 109, Feb. 2025, Art. no. 115234.

[16] L. A. Al-Haddad, L. Ibraheem, A. I. El-Seesy, A. A. Jaber, S. A. Al-Haddad, and R. Khosrozadeh, "Thermal heat flux distribution prediction in an electrical vehicle battery cell using finite element analysis and neural network," *Green Energy Intell. Transp.*, vol. 3, no. 3, Jun. 2024, Art. no. 100155.

[17] M. Sadeh et al., "A novel hybrid liquid-cooled battery thermal management system for electric vehicles in highway fuel-economy condition," *J. Energy Storage*, vol. 86, May 2024, Art. no. 111195.

[18] Y. Lai, W. Wu, K. Chen, S. Wang, and C. Xin, "A compact and lightweight liquid-cooled thermal management solution for cylindrical lithium-ion power battery pack," *Int. J. Heat Mass Transf.*, vol. 144, Dec. 2019, Art. no. 118581.

[19] Z. An, J. Zhang, W. Gao, H. Liu, and Z. Gao, "Lightweight hybrid lithium-ion battery thermal management system based on 3D-printed scaffold," *J. Energy Storage*, vol. 78, Feb. 2024, Art. no. 110141.

[20] J. H. Pu et al., "Design and performance of a compact lightweight hybrid thermal management system using phase change material and liquid cooling with a honeycomb-like structure for prismatic lithium-ion batteries," *J. Power Sources*, vol. 624, Dec. 2024, Art. no. 235632.

[21] S. S. Thakur, R. Akula, and L. Kumar, "An effective and lightweight battery thermal management system with incremental contact area: A numerical study," *Appl. Thermal Eng.*, vol. 242, Apr. 2024, Art. no. 122555.

[22] K. Li, F. Wei, K. J. Tseng, and B.-H. Soong, "A practical lithium-ion battery model for state of energy and voltage responses prediction incorporating temperature and ageing effects," *IEEE Trans. Ind. Electron.*, vol. 65, no. 8, pp. 6696–6708, Aug. 2018.

[23] S. Vashisht, D. Rakshit, S. Panchal, M. Fowler, and R. Fraser, "Experimental estimation of heat generating parameters for battery module using inverse prediction method," *Int. Commun. Heat Mass Transf.*, vol. 162, Mar. 2025, Art. no. 108539.

[24] Y. Liang, D. Bodnár, G. Ram Chandra Mouli, D. Ragni, and P. Bauer, "Charging demand prediction: Small all-electric aircraft and electric vertical takeoff and landing aircraft," *IEEE Trans. Transport. Electrific.*, vol. 11, no. 1, pp. 2732–2747, Feb. 2025.

[25] *Specification of Product for Lithium-Ion Rechargeable Cell: INR18650-35E*, Samsung SDI Co., Battery Bus. Division, 2016.

[26] M. Muratori, M. Canova, and Y. Guezennec, "A spatially-reduced dynamic model for the thermal characterisation of Li-ion battery cells," *Int. J. Vehicle Des.*, vol. 58, nos. 2–4, pp. 134–158, 2012.

[27] D. Bernardi, E. Pawlikowski, and J. Newman, "A general energy balance for battery systems," *J. Electrochem. Soc.*, vol. 132, no. 1, p. 5, 1985.

[28] K. E. Thomas and J. Newman, "Thermal modeling of porous insertion electrodes," *J. Electrochem. Soc.*, vol. 150, no. 2, p. A176, 2003.

[29] Y. Xie et al., "An improved electrothermal-coupled model for the temperature estimation of an air-cooled battery pack," *Int. J. Energy Res.*, vol. 44, no. 3, pp. 2037–2060, Mar. 2020.

[30] Y. Xie, X. Wang, X. Hu, W. Li, Y. Zhang, and X. Lin, "An enhanced electro-thermal model for EV battery packs considering current distribution in parallel branches," *IEEE Trans. Power Electron.*, vol. 37, no. 1, pp. 1027–1043, Jan. 2022.

[31] W. Vermeer, G. R. Chandra Mouli, and P. Bauer, "A comprehensive review on the characteristics and modeling of lithium-ion battery aging," *IEEE Trans. Transport. Electrific.*, vol. 8, no. 2, pp. 2205–2232, Jun. 2022.

[32] J. Zhu et al., "Data-driven capacity estimation of commercial lithium-ion batteries from voltage relaxation," *Nature Commun.*, vol. 13, no. 1, p. 2261, Apr. 2022.

[33] J. Wang et al., "Degradation of lithium ion batteries employing graphite negatives and nickel–cobalt–manganese oxide + spinel manganese oxide positives: Part 1, aging mechanisms and life estimation," *J. Power Sources*, vol. 269, pp. 937–948, Dec. 2014.
[34] G. Suri and S. Onori, "A control-oriented cycle-life model for hybrid electric vehicle lithium-ion batteries," *Energy*, vol. 96, pp. 644–653, Feb. 2016.
[35] Y. Deng et al., "Effects of different coolants and cooling strategies on the cooling performance of the power lithium ion battery system: A review," *Appl. Thermal Eng.*, vol. 142, pp. 10–29, Sep. 2018.
[36] S. Liu et al., "Thermal equalization design for the battery energy storage system (BESS) of a fully electric ship," *Energy*, vol. 312, Dec. 2024, Art. no. 133611.
[37] A. S. van Heerden, D. M. Judt, S. Jafari, C. P. Lawson, T. Nikolaidis, and D. Bosak, "Aircraft thermal management: Practices, technology, system architectures, future challenges, and opportunities," *Prog. Aerosp. Sci.*, vol. 128, Jan. 2022, Art. no. 100767.
[38] W. Affonso et al., "Thermal Management challenges for HEA–FUTPRINT 50," in *Proc. IOP Conf., Mater. Sci. Eng.*, 2021, vol. 1024, no. 1, Art. no. 012075.
[39] M. Coutinho et al., "A review on the recent developments in thermal management systems for hybrid-electric aircraft," *Appl. Thermal Eng.*, vol. 227, Jun. 2023, Art. no. 120427.
[40] (2023). *The Battery Report 2022*. Volta Foundation. [Online]. Available: https://report.volta.foundation/annual-battery-report/public/Battery_Report_2022.pdf
[41] (2020). *Pilot's Operating Handbook Velis Electro*. Pipistrel by Textron eAviation. [Online]. Available: https://www.domergue.aero/wp-content/uploads/Manuel-de-vol-Pipistrel%20-Velis-Electro.pdf
[42] G. Liao, W. Wang, F. Zhang, J. E, J. Chen, and E. Leng, "Thermal performance of lithium-ion battery thermal management system based on nanofluid," *Appl. Thermal Eng.*, vol. 216, Nov. 2022, Art. no. 118997.
[43] S. S. Shekar and M. A. Clarke, "Design and in-flight analysis of an electric aircraft's battery thermal management system," in *Proc. IEEE Transp. Electrific. Conf. Expo (ITEC)*, Jun. 2024, pp. 1–8.
[44] B. J. Yurkovich, "Electrothermal battery pack modeling and simulation," Ph.D. dissertation, Ohio State Univ., Columbus, OH, USA, 2010.
[45] D. Kim, S. Abdallahh, G. Bosi, and A. Hales, "A numerical study of the suitability of phase-change materials for battery thermal management in flight applications," *World Electr. Vehicle J.*, vol. 14, no. 1, p. 15, Jan. 2023.
[46] T. L. Bergman, A. S. Lavine, F. P. Incropera, and D. P. DeWitt, *Introduction to Heat Transfer*. Hoboken, NJ, USA: Wiley, 2011.
[47] R. Guo, J. Dong, R. E. Wolleswinkel, R. de Vries, and M. G. Niasar, "Electrical architecture of 90-seater electric aircraft: A cable perspective," *IEEE Trans. Transport. Electrific.*, vol. 11, no. 2, pp. 6854–6865, Apr. 2025.
[48] National Research Council, *Accelerated Aging of Materials and Structures: The Effects of Long-Term Elevated-Temperature Exposure*. Washington, DC, USA: The National Academies Press, 1996.
[49] D. Raymer, *Aircraft Design: A Conceptual Approach*. Reston, VA, USA: American Institute of Aeronautics and Astronautics, 2012.
[50] A. Ramesh Babu, B. Minovski, and S. Sebben, "Thermal encapsulation of large battery packs for electric vehicles operating in cold climate," *Appl. Thermal Eng.*, vol. 212, Jul. 2022, Art. no. 118548.
[51] H. Wu, X. Zhang, C. Wang, R. Cao, and C. Yang, "Experimental study on aerogel passive thermal control method for cylindrical lithium-ion batteries at low temperature," *Appl. Thermal Eng.*, vol. 169, Mar. 2020, Art. no. 114946.
[52] Z. Liu, Y. Wang, J. Zhang, and Z. Liu, "Shortcut computation for the thermal management of a large air-cooled battery pack," *Appl. Thermal Eng.*, vol. 66, nos. 1–2, pp. 445–452, May 2014.

Yawen Liang (Graduate Student Member, IEEE) received the B.Sc. degree in electrical engineering and automation from Sichuan University, Chengdu, China, in 2020, and the M.Sc. degree (cum laude) in electrical power engineering from Delft University of Technology, Delft, The Netherlands, in 2022, where she is currently pursuing the Ph.D. degree in electrical engineering with the DC Systems, Energy Conversion and Storage Group.

Her research interests include battery systems and power electronics interface for electric aircraft.

Weiming Luo received the B.Sc. degree in energy and power engineering from Xi'an Jiaotong University, Xi'an, China, in 2017, and the M.Sc. degree in sustainable energy technology from Delft University of Technology, Delft, The Netherlands, in 2024.

He graduated with a thesis on the design of a battery pack for electric aircraft. He is currently with Contemporary Amperex Technology Company Ltd. (CATL), Ningde, China, as a Thermal Simulation Engineer.

Gautham Ram Chandra Mouli (Member, IEEE) received the bachelor's degree in electrical engineering from the National Institute of Technology, Tiruchirappalli, India, in 2011, the master's degree in electrical engineering from Delft University of Technology, Delft, The Netherlands, in 2013, and the Ph.D. degree from Delft University in 2018, for the development of a solar-powered vehicle-to-grid electric vehicle charger.

He is currently an Assistant Professor with the DC Systems, Energy Conversion and Storage Group, Department of Electrical Sustainable Energy, Delft University of Technology.

Pavol Bauer (Senior Member, IEEE) received the master's degree in electrical engineering from the Technical University of Kosice, Košice, Slovakia, in 1985, and the Ph.D. degree in electrical engineering from Delft University of Technology, Delft, The Netherlands, in 1995.

He is currently a Full Professor with the Department of Electrical Sustainable Energy and the Head of the DC Systems, Energy Conversion and Storage Group, Delft University of Technology.